Fabrication of Bi_2MoO_6/ZnO hierarchical heterostructures with enhanced visible-light photocatalytic activity

Guping Zhang, Dongyun Chen[*], Najun Li, Qingfeng Xu, Hua Li, Jinghui He, Jianmei Lu[*]

Collaborative Innovation Center of Suzhou Nano Science and Technology, College of Chemistry Chemical Engineering and Materials Science Soochow University, 199 Ren'ai Road, Suzhou, 215123, PR China

ABSTRACT

The construction of heterostructures is regarded as an excellent strategy to achieve efficient charge separation and improved photocatalytic activity. Herein, a series of Bi_2MoO_6/ZnO hierarchical heterostructured photocatalysts were synthesized by a solvothermal method. The morphology of Bi_2MoO_6 grown on the surface of ZnO nanorods could be controlled by adjusting the experimental conditions. The synthesized samples were characterized by various analytical techniques and their photocatalytic performance was evaluated by photocatalytic reduction of Cr(VI) under visible-light irradiation. Compared with those of pure Bi_2MoO_6 and ZnO, the Bi_2MoO_6/ZnO composites showed higher photocatalytic activity towards the reduction of Cr(VI). The enhanced photocatalytic activity was mainly attributed to the formation of a heterojunction between Bi_2MoO_6 and ZnO, which effectively facilitated the separation and transfer of electrons and holes. In addition, the Bi_2MoO_6/ZnO photocatalysts maintained good stability after three cycles of Cr(VI) photoreduction. A possible photocatalytic mechanism of the as-synthesized composites was proposed.

1. Introduction

In the past few decades, semiconductor photocatalysts have attracted considerable research attention because of their extensive range of applications in eliminating hazardous environmental pollutants such as drugs, dyes, and heavy metals like chromium directly using solar energy [1,2]. Among the various photocatalysts considered in present research, zinc oxide (ZnO) is widely believed to be a promising photocatalytic material because of its excellent physicochemical and photonic stability, nontoxicity, and low cost [3,4]. However, pure ZnO exhibits low photocatalytic activity for two main reasons. First, ZnO has a wide band gap (E_g ~3.37 eV), so it can only absorb ultraviolet (UV) light, which greatly restricts its photocatalytic applications [5]. Second, the fast recombination rate of photoinduced electron–hole pairs in ZnO seriously decreases its photocatalytic efficiency [6]. Therefore, it is desirable to develop an efficient strategy to transfer the optical response of ZnO from the UV to the visible region and maintain its photoactivity for a long period of time.

Constructing semiconductor heterostructures of ZnO with visible light-active materials is a simple and effective method to improve its photocatalytic performance [7,8]. This is because the heterojunction interfaces in such heterostructures not only help to broaden their light-harvesting window to include visible light, but also simultaneously

lengthen charge carrier lifetimes [9,10]. Recently, Bi(III)-containing oxides have attracted extensive interest in the field of photocatalysis and energy conversion because of their layered structure and noteworthy intrinsic properties [11–13]. In particular, bismuth molybdate (Bi_2MoO_6) consists of alternating perovskite (MoO_4^{2-}) and $[Bi_2O_2]^{2+}$ layers, which give it controllable morphology and a suitable E_g (2.5–2.7 eV) to capture visible light [14–16]. Bi_2MoO_6 is a promising candidate as a cocatalyst with ZnO to hinder the recombination of photoinduced electron–hole pairs because of their well-matched E_g. For example, Tian and co-workers fabricated Bi_2MoO_6/ZnO composite nanoparticle heterojunctions that displayed dramatically enhanced photocatalytic methyl orange removal under visible light compared with the photocatalytic activities of pure ZnO and Bi_2MoO_6 [17].

Morphology and structure are also well known to influence the photocatalytic performance of catalysts [18,19]. Three-dimensional (3D) hierarchical structures consisting of two-dimensional (2D) layered nanostructure and one-dimensional (1D) materials are currently attracting great attention for adsorption and photocatalysis applications. Zhang and co-workers constructed few-layer molybdenum disulfide (MoS_2) nanosheets on titanium dioxide (TiO_2) nanobelts to provide a composite that strongly adsorbed organic dyes and completely degraded rhodamine B (RhB) (15 mg/L) within 20 min under light irradiation [20]. Lu and colleagues grew molybdenum trioxide (MoO_3)
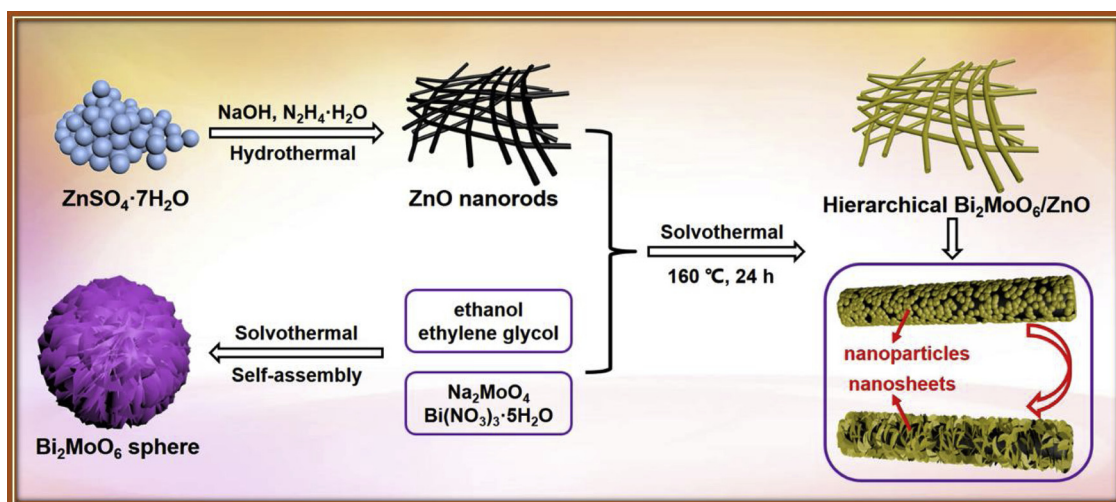
---

* Corresponding authors.
E-mail addresses: dychen@suda.edu.cn (D. Chen), lujm@suda.edu.cn (J. Lu).

Scheme 1. Schematic illustration of the fabrication of 3D Bi_2MoO_6/ZnO hierarchical composites.

with different morphologies on TiO_2 nanofibers. The resulting MoO_3 nanosheet/TiO_2 composite displayed photocatalytic RhB (10 mg/L) removal activity that was enhanced by 3.3 times compared with that of a MoO_3 nanoparticle/TiO_2 photocatalyst because of the 3D porous structure of the former [21]. According to numerous previous studies, 3D hierarchical structure can effectively improve photocatalytic performance because of the following reasons [15,18–22]: (1) 1D nanostructures, such as nanowires, nanorods, and nanotubes, in the 3D structure can provide pathways for charge transfer to promote the separation of photoinduced electron–hole pairs; (2) the 3D hierarchical structure makes full use of light by inducing multiple reflections of visible light; (3) the 3D structure can provide a large surface area and numerous active sites to facilitate adsorption and photochemical reactions.

Based on the above considerations, in this study, we synthesize a 3D Bi_2MoO_6/ZnO hierarchical heterojunction by assembling 2D Bi_2MoO_6 nanosheets on 1D ZnO nanorods through a solvothermal method (Scheme 1). The synthesized Bi_2MoO_6/ZnO composites are characterized by various analytical techniques and their photocatalytic performance is evaluated by photocatalytic reduction of Cr(VI) under visible-light irradiation. The Bi_2MoO_6/ZnO composites show higher photocatalytic activity than their individual components and exhibit good cycling stability. The possible photocatalytic mechanism for the Bi_2MoO_6/ZnO composites is discussed in detail.

2. Experiment section

2.1. Materials and Reagents

All chemicals and reagents were used as received from commercial suppliers without further purification. Absolute ethanol (C_2H_5OH), hydrazine hydrate ($N_2H_4 \cdot H_2O$, 85%), ethylene glycol (EG) were all analytical grade and purchased from Sinopharm Chemical Reagent Co. Ltd. (China). Zinc sulfate heptahydrate ($ZnSO_4 \cdot 7H_2O$), sodium hydroxide (NaOH), bismuth(III) nitrate pentahydrate ($Bi(NO_3)_3 \cdot 5H_2O$) and sodium molybdate dihydrate ($Na_2MoO_4 \cdot 2H_2O$) were bought from Sigma-Aldrich. The water used in all experiments was purified by a Millipore system (18.2 MΩ cm).

2.2. Synthesis of ZnO Nanorods

The ZnO nanorods were synthesized *via* a hydrothermal method. In a typical experimental procedure, $ZnSO_4 \cdot 7H_2O$ (600 mg) was dispersed in NaOH solution (60 mL, 0.5 M) with vigorous magnetic stirring for 30 min. Then, $N_2H_4 \cdot H_2O$ (10 mL, 85%) was added into the solution and

stirred for another 30 min. The resulting solution was transferred into a 100 mL Teflon-lined stainless steel autoclave, which was heated to 90 °C and maintained for 5 h. After cooling down to room temperature, the white precipitate was collected by centrifugation (8000 rpm, 5 min), washed thoroughly with deionized water and ethanol for several times, and finally dried at 60 °C under vacuum.

2.3. Synthesis of Bi_2MoO_6/ZnO composites

The Bi_2MoO_6/ZnO heterostructures was synthesized by a one-step solvothermal reactions [15,23]. Firstly, $Bi(NO_3)_3 \cdot 5H_2O$ (1.3 mmol) and $Na_2MoO_4 \cdot 2H_2O$ (0.65 mmol) were dissolved into 5 mL ethylene glycol by ultrasonication, respectively. Then, the two solutions were mixed and absolute ethanol (30 mL) was added into the above mixed solution under magnetic stirring 30 min. Next, ZnO nanorods (1 mmol) were dispersed into the solution and stirred for 60 min. Finally, the above mixture were transferred into 50 mL Teflon-lined stainless steel autoclave, which was heated to 160 °C for 24 h. After cooling to the room temperature, the obtained sample was rinsed with deionized water and ethanol for three times and finally dried at 80 °C for 12 h in a vacuum oven. For ease of description, the as-prepared sample with a Bi_2MoO_6/ZnO molar ratio of 0.65/1 were named as BZ-0.65. By changing the precursor concentration, three other samples of Bi_2MoO_6/ZnO were fabricated and denoted as BZ-0.16, BZ-0.33 and BZ-0.98. Moreover, pure Bi_2MoO_6 nanosheets were also synthesized by a similar method without adding ZnO nanorods.

2.4. Characterization

The structure and crystallinity of the synthesized composites were analyzed by X-ray diffraction (XRD) and carried out on a X'Pert-Pro MPD. The morphologies and microstructures of the composites were characterized by Transmission electron microscopy (TEM, Tecnai G200) and Scanning electron microscopy (SEM, Hitachi S-4700). The chemical status, elemental composition and the valence band (VB) edges of photocatalysts were determined using an X-ray photoelectron spectrometer (ESCALAB MK II) with Al-Kα radiation. The specific surface area tests were performed with a Micromeritics ASAP 2010 system and analyzed by the Brunauer-Emmett-Teller (BET) method. The optical properties of the synthesized materials were obtained using a spectrophotometer (UV–vis, DRS Shimadzu UV-3600). The photocurrent and the electrochemical impedance spectra (EIS) were recorded by an electrochemical workstation (CHI660E, China) with a three-electrode cell system, and the detailed process was displayed in the Supporting Information S1.

2.5. DFT calculation

The density functional theory (DFT) calculations were used to study the band structure and the density of states (DOS) of ZnO and Bi_2MoO_6, and carried out by CASTEP module within the plane-wave pseudopotential method [24–26]. The exchange-correlation function was modeled using the generalized gradient approximation (GGA) with Perdew-Burke-Ernzerh (PBE). The cut-off energy of the plane-wave expansion was set to 600 or 400 eV with thresholds of energy 10^{-6} eV and force 0.01 eV Å^{-1}, The Brillouin zone was sampled with a Monkhorst and Pack k-point grid of $9 \times 9 \times 6$ for ZnO and $2 \times 2 \times 5$ for Bi_2MoO_6.

2.6. Photocatalytic activity experiments

In a typical experiment, 100 mg of as- synthesized catalysts were firstly added into 50 mL of Cr(VI) solution (50 mg/L, based on Cr in $K_2Cr_2O_7$ solution). Then, the pH of initial solution was adjusted to 2 using a 1 M H_2SO_4 solution. Before irradiation, the suspension was stirred for 60 min in darkness to establish an adsorption-desorption equilibrium. During the xenon lamp (300 W, $\lambda > 400$ nm) irradiation, 1.5 mL of suspension was sampled from the reactor at a fixed time interval with a 0.22 μm membrane filter syringe to remove the residual particles. At last, the Cr(VI) concentration was measured at the absorbance of 540 nm using diphenylcarbazide (DPC) method (**Supporting Information S2**). In order to study the effect of solution pH on photocatalytic efficiency, the pH of Cr(VI) initial solution was adjusted by 1 M H_2SO_4 or 1 M NaOH solution.

3. Results and discussion

3.1. XRD analysis

X-ray diffraction (XRD) was used to investigate the crystallographic structure and phase composition of the as-synthesized samples. As shown in Fig. 1, all characteristic diffraction peaks of the pure ZnO nanorods were consistent with hexagonal wurtzite ZnO (JCPDS card no. 36-1451) [27]. The diffraction peaks observed at $2\theta = 28.31°$, 32.53°, 46.74°, 55.44°, and 58.48° for the Bi_2MoO_6 nanosheets were assigned to the (131), (200), (202), (331), and (262) crystal planes of orthorhombic Bi_2MoO_6 (JCPDS card no. 21-0102), respectively [13–15]. For the Bi_2MoO_6/ZnO composites, the characteristic diffraction peaks of both ZnO and Bi_2MoO_6 were all clearly observed without shifts of positions. As the Bi_2MoO_6/ZnO molar ratio increased from 0.16 to 0.98, the intensities of the characteristic peaks of ZnO gradually weakened, whereas those for Bi_2MoO_6 gradually strengthened. Based on the above results, Bi_2MoO_6/ZnO composites that integrated orthorhombic Bi_2MoO_6 nanostructures with wurtzite ZnO were successfully obtained by the solvothermal method. No impurity peaks were observed, confirming the high purity of the as-synthesized samples.
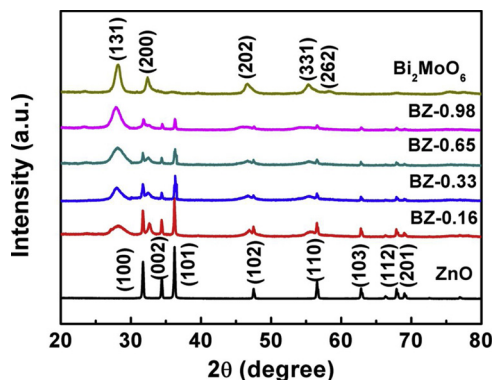

Fig. 1. XRD patterns of ZnO nanorods, Bi_2MoO_6 nanosheets, and Bi_2MoO_6/ZnO composites with different compositions.

3.2. SEM and TEM analyses

The morphologies of ZnO, Bi_2MoO_6, and Bi_2MoO_6/ZnO samples were investigated by scanning electron microscopy (SEM). As displayed in Fig. 2a and **S1**, the synthesized ZnO nanorods possessed a diameter of about 300 nm and length of several micrometers with a relatively smooth surface, providing a suitable environment to host a co-photocatalyst. Fig. 2**b–e** show that Bi_2MoO_6 with different morphologies depending on the Bi_2MoO_6/ZnO molar ratio was coated on the surface of the ZnO nanorods in the solvothermal process. Fig. 2**b** reveals that numerous Bi_2MoO_6 nanoparticles grew on the external surface of the ZnO nanorods, confirming the existence of high-energy nucleation sites suitable for growing Bi_2MoO_6 nanocrystals on the outside of the ZnO nanorods [15,18]. With increasing content of the Bi_2MoO_6 precursor, the morphology of Bi_2MoO_6 coated on the ZnO nanorods changed from nanoparticles to nanosheets (Fig. 2**c** and **d**). When the Bi_2MoO_6/ZnO molar ratio was 0.65, the entire surface of the 1D ZnO nanorods was covered with uniform 2D Bi_2MoO_6 ultrathin nanosheets. The numerous Bi_2MoO_6 nanosheets were connected with each other to form a 3D hierarchical core–shell structure. Such 3D hierarchical structure may provide abundant active sites for adsorption and photocatalytic reaction of substrate molecules [19,20,23]. However, when the $Bi(NO_3)_3$ and Na_2MoO_4 concentrations were increased further, some Bi_2MoO_6 agglomerates formed on the surface of the Bi_2MoO_6/ZnO sample (Fig. 2e). Agglomerate formation was attributed to the rapid nucleation of Bi_2MoO_6 at high precursor concentration. For comparison, an SEM image of pure Bi_2MoO_6 is depicted in Fig. 2**f**. Without ZnO nanorods as a substrate, the pure Bi_2MoO_6 nanosheets self-assembled into spheres with rough surfaces.

Subsequently, TEM was employed to observe the structure and composition of the Bi_2MoO_6/ZnO composites using the BZ-0.65 sample as the model. As shown in Fig. 3a, Bi_2MoO_6 in BZ-0.65 had a thin sheet-like structure and uniformly covered the surface of the ZnO nanorods. An intimate interface between Bi_2MoO_6 and ZnO in BZ-0.65 is clearly displayed in Fig. 3**b**. The lattice fringes with *d*-spacings of 0.246 and 0.316 nm are assigned to the (101) lattice plane of hexagonal wurtzite ZnO and (131) plane of orthorhombic Bi_2MoO_6, respectively [15,27,28]. EDX elemental mapping was then used to study the elemental composition and distribution of the synthesized BZ-0.65 sample, as illustrated in Fig. 3**c**. The elemental mapping images indicated that the prepared BZ-0.65 sample contained Zn, O, Bi, and Mo. Furthermore, the EDX mapping analysis of Bi_2MoO_6/ZnO also revealed the core (ZnO nanorods)–shell (Bi_2MoO_6 nanosheets) structure of the BZ-0.65 sample. The results of SEM and TEM analyses confirmed the successful formation of Bi_2MoO_6/ZnO core–shell hierarchical heterojunctions with fibrous morphology in the BZ-0.65 sample.

3.3. EDS and XPS analyses

The surface composition and chemical states of BZ-0.65 were further studied by EDS and XPS. The EDS and survey XPS curves in Fig. 4**a** and **b**, respectively, indicated that the BZ-0.65 sample consisted of Bi, Mo, Zn, and O, which is in good agreement with the mapping analysis (see Fig. 3c). The high-resolution Bi 4f, Mo 3d, Zn 2p, and O 1 s spectra obtained for BZ-0.65 are shown in Fig. 4**c–f**. As depicted in Fig. 4c, two strong peaks in the Bi 4f region at 158.9 and 164.2 eV were assigned to Bi $4f_{7/2}$ and Bi $4f_{5/2}$ of Bi^{3+}, respectively [19,22]. The peaks located at binding energies of around 232.1 and 235.2 eV (Fig. 4d) corresponded to the Mo $3d_{5/2}$ and Mo $3d_{3/2}$ states of Mo^{6+} in Bi_2MoO_6, respectively [16]. Fig. 4**e** contained peaks at 1021.5 and 1044.6 eV that were characteristic of Zn $2p_{3/2}$ and Zn $2p_{1/2}$, respectively [3]. Moreover, it was worth mentioning that the binding energies of Zn 2p for BZ-0.65 sample were higher than those of pure ZnO (**Figure S2**), indicating electron migration through the interface of Bi_2MoO_6 and ZnO [7]. Such a similar phenomenon is also observed from the XPS spectra of Bi 4f and Mo 3d peaks (**Figure S2**). This behavior was beneficial for charge
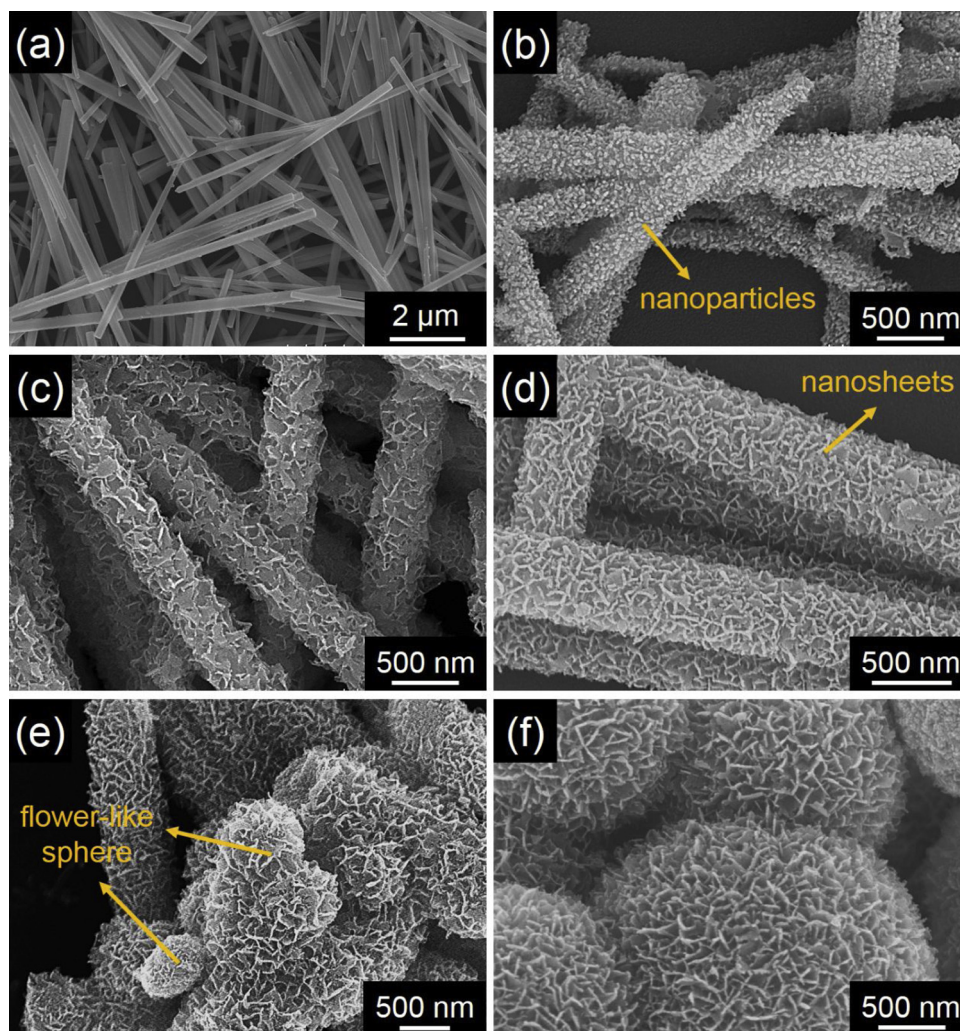
Fig. 2. SEM images of (a) pure ZnO nanorods, (b–e) Bi_2MoO_6/ZnO composites with different compositions: (b) 0.16/1, (c) 0.33/1, (d) 0.65/1 (e) 0.98/1 and (f) pure Bi_2MoO_6 spheres assembled from Bi_2MoO_6 nanosheets.

separation and enhancement of photocatalytic activity [7,8]. The high-resolution O 1 s spectrum (Fig. 4f) was fitted with four peaks. The peak at 531.8 eV was indexed to O−H bonds originating from adsorbed H_2O molecules. The other three peaks at 530.8, 530.1, and 529.6 eV were consistent with Mo-O, Zn-O, and Bi-O bonds, respectively, further verifying the successful growth of Bi_2MoO_6 on ZnO nanorods [5,7,29]. Therefore, the XPS results provided further evidence for the coexistence of ZnO and Bi_2MoO_6 in the Bi_2MoO_6/ZnO composite, which agreed well with the XRD and HRTEM results.

3.4. BET surface area analysis

Surface area generally strongly influences the adsorption and catalytic performance of photocatalysts. Nitrogen absorption–desorption isotherms were collected to further characterize ZnO, Bi_2MoO_6, and the Bi_2MoO_6/ZnO composites. As displayed in Fig. 5, the BET specific surface areas of pure ZnO and Bi_2MoO_6 were 17.38 and 37.17 $m^2 g^{-1}$, respectively. Growth of Bi_2MoO_6 on the surface of the ZnO nanorods increased the surface areas of the Bi_2MoO_6/ZnO composites compared with that of pure ZnO. The Bi_2MoO_6/ZnO composites showed type-IV isotherms with hysteresis loops according to the IUPAC classification. The hysteresis loops observed at relative pressures (P/P_0) between 0.4 and 1.0 indicated the presence of large mesopores [23]. The mesoporous structure of the Bi_2MoO_6/ZnO composites could be formed through the assembly of the Bi_2MoO_6 nanoparticles or nanosheets. The

high surface areas and mesoporous structures of the Bi_2MoO_6/ZnO composites may provide numerous active sites to enhance their adsorption ability and photocatalytic activity.

3.5. DFT analysis

The band structures and density of states (DOS) of ZnO and Bi_2MoO_6 were calculated using the density functional theory (DFT) method. The crystal structure models of ZnO and Bi_2MoO_6 used in the DFT calculations are shown in **Figure S3**. Fig. 6a and **c** clearly reveal that both ZnO and Bi_2MoO_6 are direct band-gap semiconductors because the valence band maximum (VBM) and conduction band minimum (CBM) of each material are situated at the same high-symmetry G point, which is in accordance with previous reports [24,26]. Fig. 6**b** illustrates that the VBM of ZnO mainly consists of Zn 3d, O 2 s, and O 2p orbitals and its CBM is composed of Zn 3 s and Zn 3p orbitals. Meanwhile, the VBM of Bi_2MoO_6 is mainly composed of Bi 6 s, O 2 s, and O 2p orbitals, whereas its CBM is mainly consists of hybridized Bi 6p, Mo 4d, and O 2p orbitals. The calculated E_g for ZnO and Bi_2MoO_6 are 3.004 and 2.218 eV, respectively. The calculated E_g values are smaller than the experimental results (Fig. 7b), which is probably because of the limitation of DFT calculations [24–26,30].
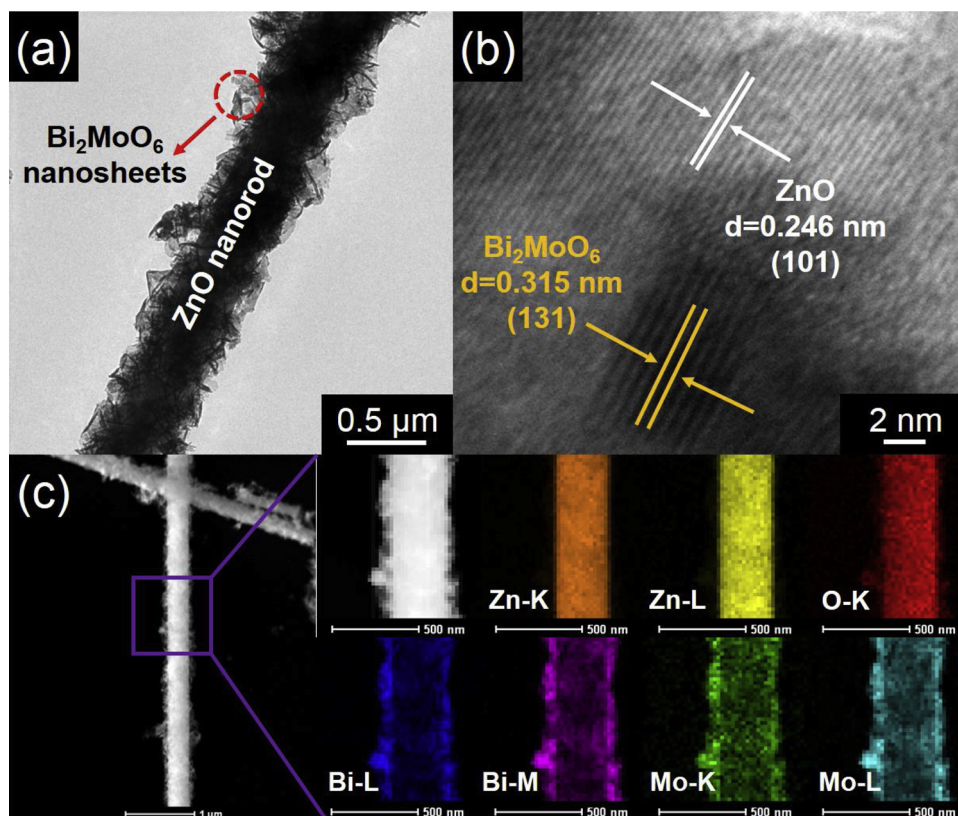
Fig. 3. (a) Typical TEM image of the BZ-0.65 sample, (b) HRTEM image taken at the interface between Bi_2MoO_6 and ZnO, and (c) HAADF-STEM/EDX mapping images of the BZ-0.65 sample.

3.6. Optical absorption behavior and band gap positions

The optical properties of the as-synthesized samples were investigated by UV − vis diffuse reflectance spectroscopy (DRS). Fig. 7a illustrates that the absorption edge of pristine ZnO is around 400 nm, which is caused by its wide E_g. In contrast, pure Bi_2MoO_6 exhibited an absorption edge at about 475 nm, which is in accordance with previous reports and indicates light harvesting in both the UV and visible regions. As expected, the Bi_2MoO_6/ZnO composites displayed markedly improved capability to absorb visible light compared with that of ZnO. A red shift of the absorption wavelength was observed for the Bi_2MoO_6/ZnO composites with increasing Bi_2MoO_6 proportion. The enhanced visible-light absorption of the Bi_2MoO_6/ZnO composites compared with that of ZnO can generate more electrons and holes needed for the photocatalytic reaction [19,22,23]. In addition, E_g of ZnO and Bi_2MoO_6 were calculated according to the Kubelka–Munk function (Equation 1):

$$\alpha h\nu = A(h\nu - E_g)^{n/2} \tag{1}$$

where α, hν, and A are the absorption coefficient, discrete photon energy, and a constant, respectively. Meanwhile, n is determined by the type of optical transition in the semiconductor (n = 1 for a direct transition, n = 4 for an indirect transition). Both ZnO and Bi_2MoO_6 are direct-transition semiconductors, so their n values are 1 [7,15]. Plots of $(\alpha h\nu)^2$ versus hν for ZnO and Bi_2MoO_6 are shown in Fig. 7b. Evaluated E_g of ZnO and Bi_2MoO_6 were approximately 3.13 and 2.63 eV, respectively, which are close to previously reported values.

To further study the energy-band structure of the composites, XPS valence band (VB) spectra were collected and linear extrapolation was carried out to confirm the VB positions (E_{VB}) of samples. As displayed in Fig. 7c, the VB positions of ZnO and Bi_2MoO_6 were at 2.24 and 2.97 eV, respectively. According to the equation:

$$E_{CB} = E_{VB} - E_g \tag{2}$$

the corresponding conduction-band (CB) positions (E_{CB}) of ZnO and Bi_2MoO_6 are −0.16 and −0.39 eV, respectively. The resulting band structures of ZnO and Bi_2MoO_6 are presented in Fig. 7d. This figure clearly illustrated that ZnO and Bi_2MoO_6 can form a heterojunction because of their well-matched band structure. Such a heterojunction should allow the effective separation of electrons and holes, which should accordingly increase the photocatalytic activity of the composites.

3.7. Photoelectrochemical properties

To explore the influence of heterostructure on photocatalytic activity, the interface charge transfer and separation efficiency of the samples were characterized by a photoelectrochemical technique. Fig. 8a shows the transient photocurrent responses of Bi_2MoO_6 and Bi_2MoO_6/ZnO composites during several cycles of visible-light illumination being turned on and off. Pristine ZnO showed no photocurrent response since ZnO in this work could not be excited by visible light irradiation (λ > 400 nm, energy less than 3.1 eV) [19,31]. The photocurrent response of Bi_2MoO_6 was also low, which was attributed to the fast recombination of charge carriers. In contrast, the photocurrents of all Bi_2MoO_6/ZnO composites were higher than that of pure Bi_2MoO_6, indicating that the efficiency of interfacial charge transfer was increased by combining ZnO and Bi_2MoO_6. BZ-0.65 showed the highest photocurrent of the Bi_2MoO_6/ZnO composites, which was 5.3 times higher that of pure Bi_2MoO_6.

Electrochemical impedance spectroscopy (EIS) was also performed to study the separation and recombination efficiency of electron–hole pairs. As depicted in Fig. 8b, smaller arcs were observed for the Bi_2MoO_6/ZnO composites than for ZnO, which indicates decreased interfacial charge transfer resistance and suggests that the recombination of electrons and holes is inhibited in the composites [2,24]. Consequently, it can be concluded that the construction of a heterogeneous
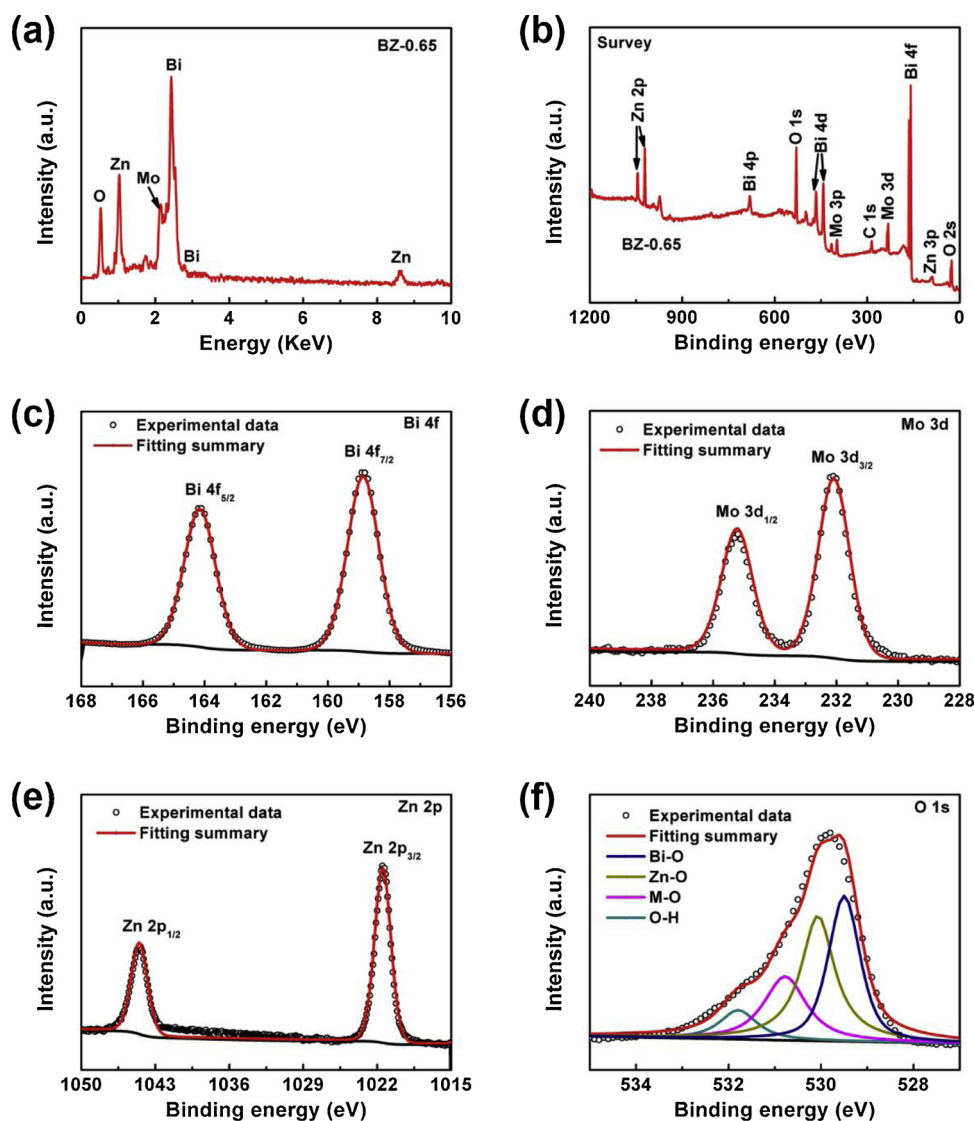
Fig. 4. (a) EDS analysis of the BZ-0.65 sample. XPS analysis of BZ-0.65 showing (b) survey, (c) Bi 4f, (d) Mo 3d, (e) Zn 2p, and (f) O 1 s spectra.
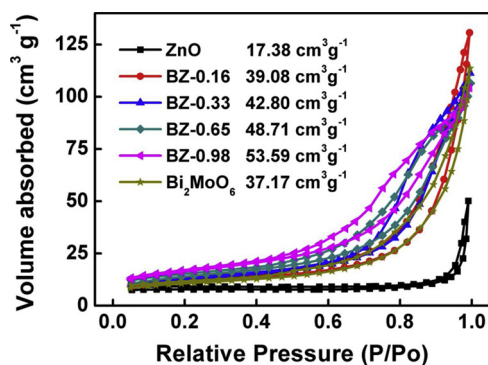

Fig. 5. N_2 adsorption–desorption isotherms of ZnO, Bi_2MoO_6, and Bi_2MoO_6/ZnO composites with different compositions.

structure of ZnO and Bi_2MoO_6 can effectively facilitate the separation and transfer electrons and holes, which should contribute to the enhancement of photocatalytic activity. It is expected that BZ-0.65 will exhibit the highest photocatalytic activity of the samples because it has the highest separation efficiency of electron–hole pairs.

3.8. Photocatalytic activity

Numerous previous reports have revealed that initial solution pH strongly affects photocatalytic Cr(VI) reduction. Therefore, the photocatalytic reduction of Cr(VI) with different initial solution pH using BZ-0.65 as the photocatalyst was conducted; the results are depicted in Fig. 9. BZ-0.65 displayed the highest photocatalytic reduction efficiency under acidic conditions (Fig. 9a). Almost 100% removal of Cr(VI) was observed when the initial pH was 2.01. The Cr(VI) removal efficiency continuously decreased with increasing pH of the initial solution. When the pH was increased to 10.50, the total removal rate of Cr(VI) decreased considerably to 14.86% (adsorption rate = 9.81% and reduction rate = 5.05%). These results are also presented in the corresponding UV–vis absorption spectra (Fig. 9**b–d** and **S4**). The reasons for the above results are as follows. First, Cr(VI) exists mainly as $Cr_2O_7^{2-}$ and $HCrO_4^-$ under acidic conditions and as CrO_4^{2-} under alkaline conditions [32]. When the initial solution pH is low, the surface of the photocatalyst is positively charged because of protonation, which is beneficial to facilitate the adsorption process through electrostatic attraction [33]. Second, the reactions that occur in acidic solutions are:
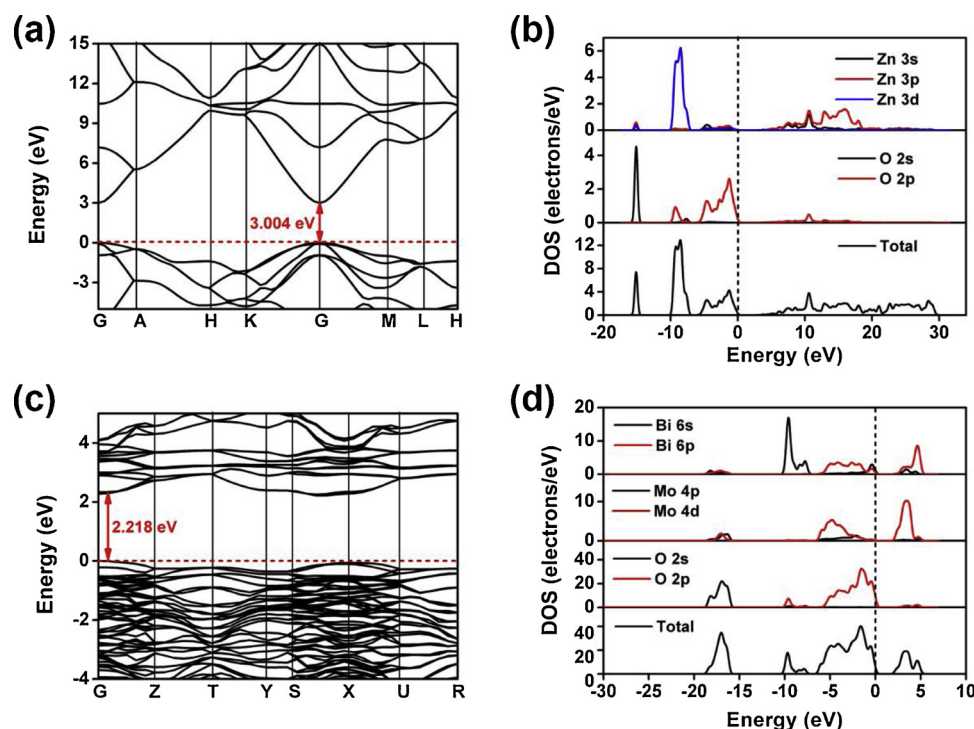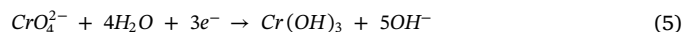
$$Cr_2O_7^{2-} + 14H^+ + 6e^- \rightarrow 2Cr^{3+} + 7H_2O \tag{3}$$

$$HCrO_4^- + 7H^+ + 3e^- \rightarrow Cr^{3+} + 4H_2O \tag{4}$$
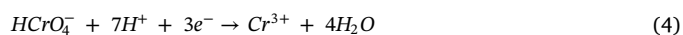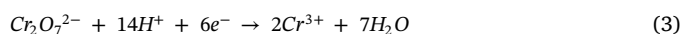
Fig. 6. Band structures of (a) ZnO and (c) Bi_2MoO_6 and density of states (DOS) of (b) ZnO and (d) Bi_2MoO_6.

The reaction that occurs in alkaline solutions is:

$$CrO_4^{2-} + 4H_2O + 3e^- \rightarrow Cr(OH)_3 + 5OH^- \qquad (5)$$

The Nernst reduction potentials of $Cr_2O_7^{2-}/Cr^{3+}$ (1.23 V vs. NHE) and $HCrO_4^-/Cr^{3+}$ (1.35 V vs. NHE) in acidic solutions are more positive than that of CrO_4^{2-}/Cr^{3+} (−0.13 V vs. NHE) in alkaline solutions [32,34]. Therefore, $Cr_2O_7^{2-}$ and $HCrO_4^-$ are easier to reduce than CrO_4^{2-} because of the larger thermodynamic driving force. Third, the Nernst equation in acidic solutions can be expressed as:

$$\varphi = \varphi^\theta + \frac{0.059}{6} lg \frac{[Cr_2O_7^{2+}]^4 \cdot [H^+]^{14}}{[Cr^{3+}]^2 \cdot [H_2O]^7} \qquad (6)$$

According to Equation 6, as the concentration of protons (H^+) increases, the value of φ increases. In addition, the equilibrium (Equation 3) will shift to the right, meaning that Cr(VI) is more easily reduced in an acidic environment than in a basic one [35]. Fourth, under alkaline conditions, Cr^{3+} deposits on the photocatalyst surface in the form of Cr(OH)$_3$ (Equation 5), which can block active sites available for adsorption and photocatalytic reactions. Overall, the photocatalytic reduction of Cr(VI) consumes H^+ and acidic conditions are more favorable for Cr
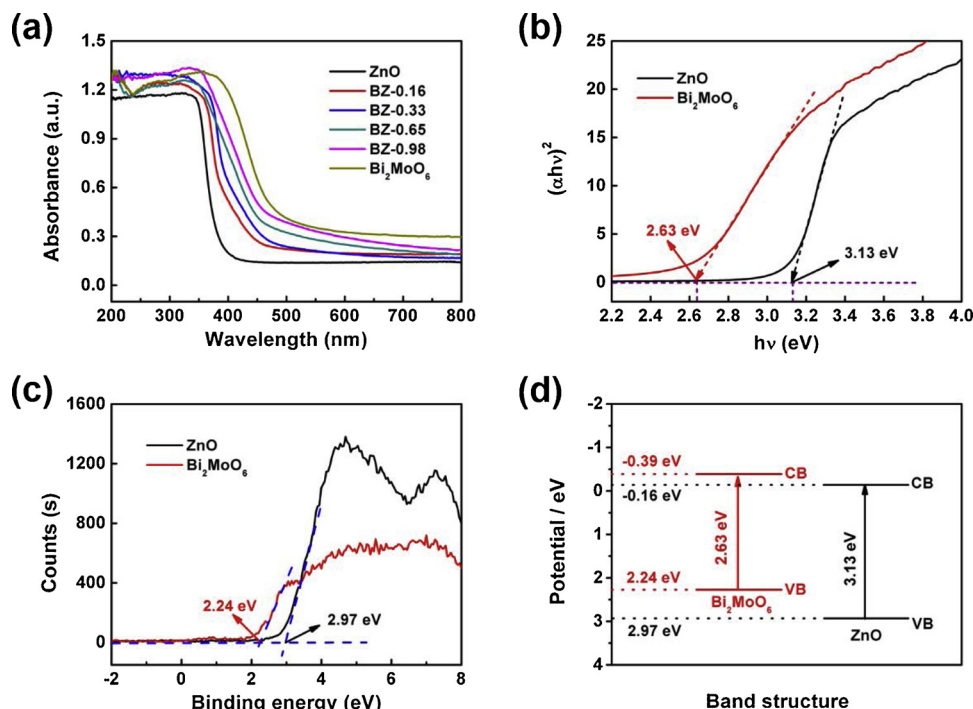

Fig. 7. (a) UV–vis diffuse reflectance spectra of ZnO, Bi_2MoO_6, and Bi_2MoO_6/ZnO composites with different compositions. (b) Plots of $(\alpha h\nu)^2$ versus ($h\nu$) used to estimate the optical band gaps of ZnO and Bi_2MoO_6. (c) Valence-band spectra of ZnO and Bi_2MoO_6. (d) Band structures of ZnO and Bi_2MoO_6. VB is valence band, CB is conduction band.
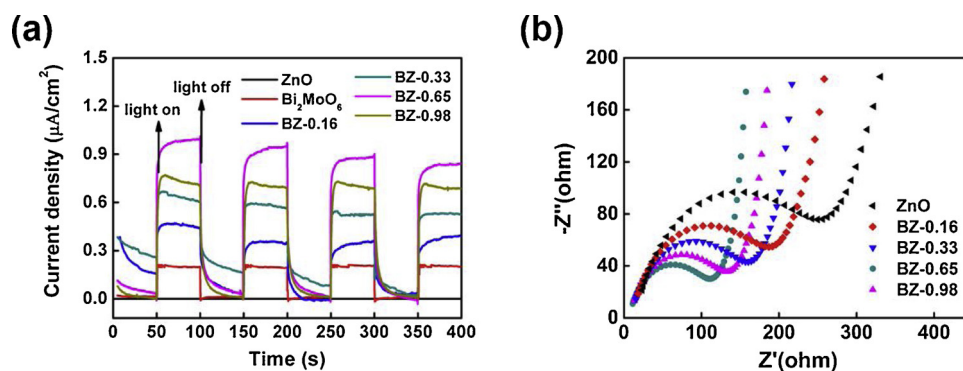
Fig. 8. (a) Transient photocurrent responses and (b) EIS analysis of ZnO, Bi_2MoO_6, and Bi_2MoO_6/ZnO composites with different compositions.

(VI) reduction than basic ones. Moreover, the solution after the photocatalytic reduction of Cr(VI) over BZ-0.65 sample was detected using ICP-MS, in order to confirm the content of Zn^{2+}, Bi^{3+} and Mo^{6+} ions in solution. The results showed that the contents of Zn^{2+}, Bi^{3+} and Mo^{6+} ions were very low (**Table S1**) in solution at pH 2.01–10.50, indicating the ions leaching from BZ-0.65 sample is insignificant. It means that the Bi_2MoO_6/ZnO composite has good chemical stability due to the strong heterostructure between ZnO and Bi_2MoO_6 [38]. Therefore, based on these considerations, the photocatalytic activities of ZnO, Bi_2MoO_6/ZnO composites, and Bi_2MoO_6 were tested by the photocatalytic reduction of Cr(VI) at pH 2.

The catalytic performances of the pure ZnO, Bi_2MoO_6, and different Bi_2MoO_6/ZnO composites were evaluated by photocatalytic reduction of Cr(VI) under visible-light irradiation. In the experiments, ZnO mechanically mixed with Bi_2MoO_6 (with a Bi_2MoO_6/ZnO molar ratio of 0.65:1, denoted as PM-BZ-0.65) was used as comparative sample to investigate the effect of the Bi_2MoO_6/ZnO heterojunction. The temporal change in the concentration of Cr(VI) was detected by measuring the maximum absorption of Cr(VI) at 540 nm by UV–vis spectroscopy (**Figure S5**). Before irradiation, the photocatalyst was stirred in the Cr (VI) solution for 60 min in the dark to achieve adsorption–desorption equilibrium. As displayed in Fig. 10a, the Bi_2MoO_6/ZnO composites showed enhanced Cr(VI) adsorption performance compared with those

of ZnO and Bi_2MoO_6, which could be ascribed to the higher BET surface areas of the composites. In the photocatalytic reduction process, pure ZnO exhibited no photocatalytic activity under visible-light irradiation. After irradiation for 150 min, the reduction rates of Cr(VI) over Bi_2MoO_6 and PM-BZ-0.65 were just 22.78% and 14.61%, respectively. In contrast, all the Bi_2MoO_6/ZnO composites exhibited the higher photocatalytic activity under the same conditions. In particular, the BZ-0.65 sample showed the highest photocatalytic activity and the corresponding reduction rates of Cr(VI) was up to 100%. This improved photocatalytic performance of the Bi_2MoO_6/ZnO composites was mainly attributed to the construction of 3D heterojunctions between Bi_2MoO_6 and ZnO, which promoted the interfacial separation of electrons and holes during photocatalysis [18,20,22]. Additionally, the solution after the photocatalytic reduction of Cr (VI) over BZ-0.65 sample was detected using ICP-MS with Cr(III) standard curve, in order to confirm the content of Cr ions in solution. The results show that the contents of Cr ions are 0.025 mg/L, which indicate the Cr(III) was mainly located on the surface of photocatalyst rather than in solution.

Photoluminescence (PL) emission spectra were measured to reveal the migration and recombination processes of the electron–hole pairs. Compared with the responses of pure ZnO and Bi_2MoO_6, BZ-0.65 showed lower PL intensity, suggesting the enhanced electron transfer between the interfaces of the two components in the composite (**Figure**
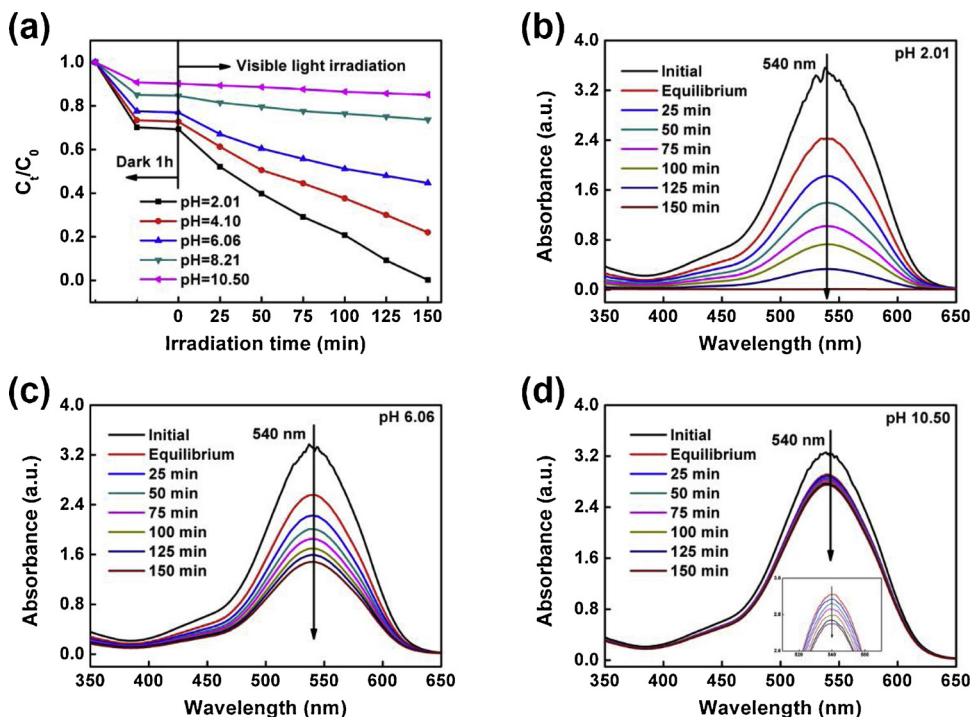

Fig. 9. (a) Effect of initial solution pH on Cr (VI) photoreduction by BZ-0.65 under visible-light irradiation. The UV–vis absorption spectral changes of Cr(VI) solution over the BZ-0.65 sample at pH of (b) 2.01, (c) 6.06, and (d) 10.50. Reaction conditions: Cr(VI) concentration = 50 mg/L, catalyst dosage = 2 g/L, light intensity = 300 W (Xe lamp, $\lambda > 400$ nm).
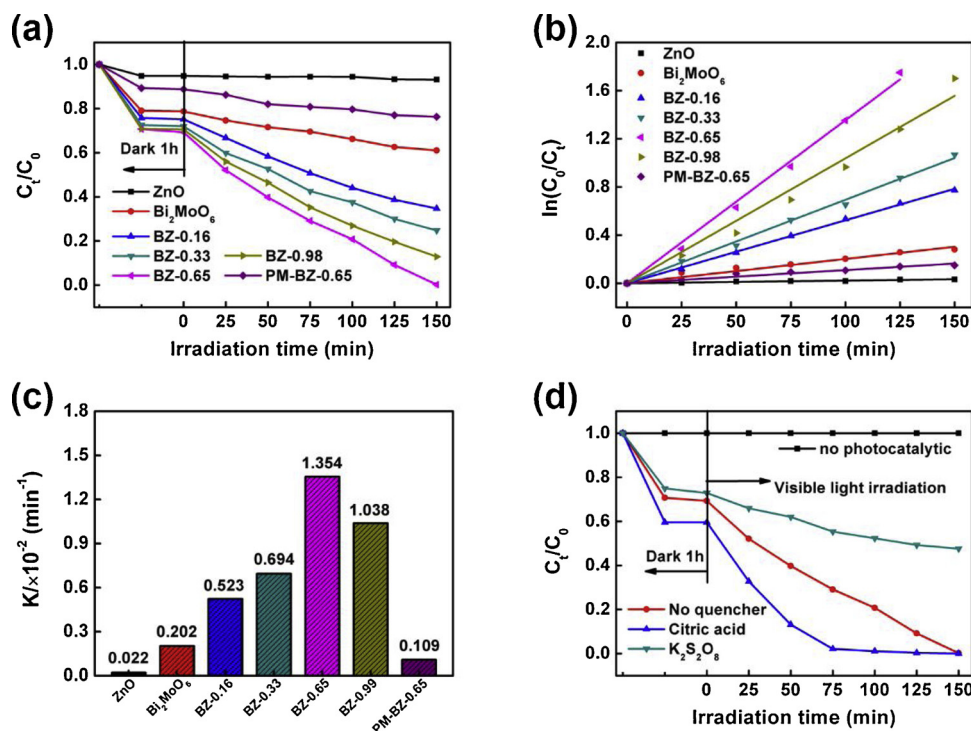
Fig. 10. (a) Photocatalytic reduction of Cr(VI) over different catalysts under visible-light irradiation. Reaction conditions: Cr(VI) concentration = 50 mg/L, catalyst dosage = 2 g/L, pH = 2, light intensity = 300 W (Xe lamp, λ > 400 nm). (b, c) Corresponding pseudo-first-order kinetics fitting curves and apparent rate constants over different catalysts. (d) Photocatalytic reduction of Cr(VI) by BZ-0.65 sample in the presence of an electron scavenger ($K_2S_2O_8$) and hole scavenger (citric acid). The dosages of $K_2S_2O_8$ and citric acid were 100 μL of 50 mg/mL aqueous solutions of $K_2S_2O_8$ and citric acid, respectively.

S6). Furthermore, the Bi_2MoO_6/ZnO molar ratio played an important role in determining the photocatalytic activity of the composites. Compared to the case for nanoparticles on ZnO nanorods (BZ-0.16), the space between the 2D nanosheets in BZ-0.33 and BZ-0.65 can induce multiple reflection of the visible light [15], which leads to more efficient absorption of light and promotes the photocatalytic reaction. However, when the Bi_2MoO_6 content of the composite was high (BZ-0.98), some Bi_2MoO_6 spheres agglomerated on the surface of the Bi_2MoO_6/ZnO composite, which may cover some of the active sites and hinder contact between Cr(VI) and the photocatalyst. In addition, excess Bi_2MoO_6 acted as recombination centers for electron–hole pairs, which was verified by the photoelectrochemical measurements (Fig. 8).

Fig. 10**b** shows the photocatalytic degradation kinetic curves of Cr(VI) by the as-prepared samples and corresponding apparent reaction rate constants (k) are presented in Fig. 10**c**. All the kinetic data fitted straight lines and obeyed the pseudo-first-order model:

$$l\,n(C_0/C_t) = kt \qquad (7)$$

where t is the irradiation time (min) and C_t and C_0 are the concentration at t and initial concentration of Cr(VI) (mg/L), respectively. BZ-0.65 displayed the highest k value, which was almost 6.7 and 12.4 times higher than those of Bi_2MoO_6 and PM-BZ-0.65, respectively. Finally, Fig. 10**d** displays the effects of an electron scavenger (potassium persulfate, $K_2S_2O_8$) and hole scavenger (citric acid) on the photocatalytic reduction of Cr(VI) by BZ-0.65. First, Cr(VI) displayed good stability under visible-light irradiation for a long time in the absence of a photocatalyst. After adding the electron scavenger $K_2S_2O_8$ to the photocatalytic system, the adsorption efficiency of Cr(VI) by BZ-0.65 decreased slightly, indicating the addition of $K_2S_2O_8$ cannot significantly change the adsorption efficiency of Cr(VI), which is consistent with the reported literatures [36,37]. However, the photocatalytic reduction efficiency of Cr(VI) decreased markedly, suggesting that electrons are the main reactive species in photocatalytic degradation of Cr(VI) [37]. In contrast, when the experiment was conducted in the presence of citric acid as a hole scavenger, the surface of the photocatalyst became more positive and negatively charged $HCrO_4^-$ or $Cr_2O_7^{2-}$ ions were preferentially adsorbed [33]. As a result, the adsorption efficiency of Cr(VI) by BZ-0.65 increased obviously. Meanwhile, the photoreduction

rate of Cr(VI) was also obviously faster, taking half the reaction time of that needed without citric acid. The main reason for the enhanced photocatalytic efficiency in the presence of citric acid may be that citric acid was adsorbed on the photocatalyst surface and easily oxidized by photogenerated holes, thus consuming numerous holes and greatly inhibiting the recombination of electron–hole pairs [38]. In addition, the citric acid may also lead to its visible-light photocatalytic degradation *via* a charge-transfer-complex path [39] and then enhance the efficiency of reduction Cr(VI). The UV–vis absorption spectral changes of Cr(VI) in the scavenger experiments are presented in **Figure S7**. Furthermore, compared with other reported visible light photocatalysts (**Table S2**), the prepared Bi_2MoO_6/ZnO composite displayed a relatively satisfactory photocatalytic activity.

To evaluate the photocatalytic stability of the Bi_2MoO_6/ZnO composites, recycling experiments of BZ-0.65 in Cr(VI) photoreduction were performed. As displayed in Fig. 11a, the Cr(VI) photodegradation activity of the BZ-0.65 sample did not drop obviously with increasing cycle number. The photoreduction rate of Cr(VI) was still 93.87% after three cycles. The corresponding UV–vis absorption spectral changes of Cr(VI) in the second and third cycle are presented in **Figure S8**. The stability of photo-reduction efficiency was mainly attributed to the porous heterostructures. The space between the 2D nanosheets in BZ-0.65 could form large mesopores structure, which facilitated the deposition of Cr(III) into the interior of large mesopores rather than the surface of the photocatalyst. As a result, the deactivation of photocatalysts was effectively suppressed during the photocatalytic cycle reduction of Cr(VI). Moreover, XRD analysis of the composite sample after use in three photocatalytic cycles (BZ-0.65-AP) revealed that the locations of characteristic peaks were not shifted compared with those of the initial sample, as shown in Fig. 11**b**. The core–shell structure of the sample was also retained after three photocatalytic cycles (**Figure S9**). The recycled BZ-0.65-AP was further characterized by XPS. The survey spectrum contained signals from Bi, Mo, O, and Zn as well as Cr contaminants (Fig. 11c). The high-resolution Cr spectrum of BZ-0.65-AP is illustrated in Fig. 11**d**. The binding energy peak of Cr $2p_{3/2}$ was observed at 577.14 eV, which is consistent with Cr(III) in Cr(OH)$_3$ [40,41]. The above results reveal that the Bi_2MoO_6/ZnO composite has good stability and can effectively reduce Cr(VI) to Cr(III) under visible-

G. Zhang, et al.

Applied Catalysis B: Environmental 250 (2019) 313–324
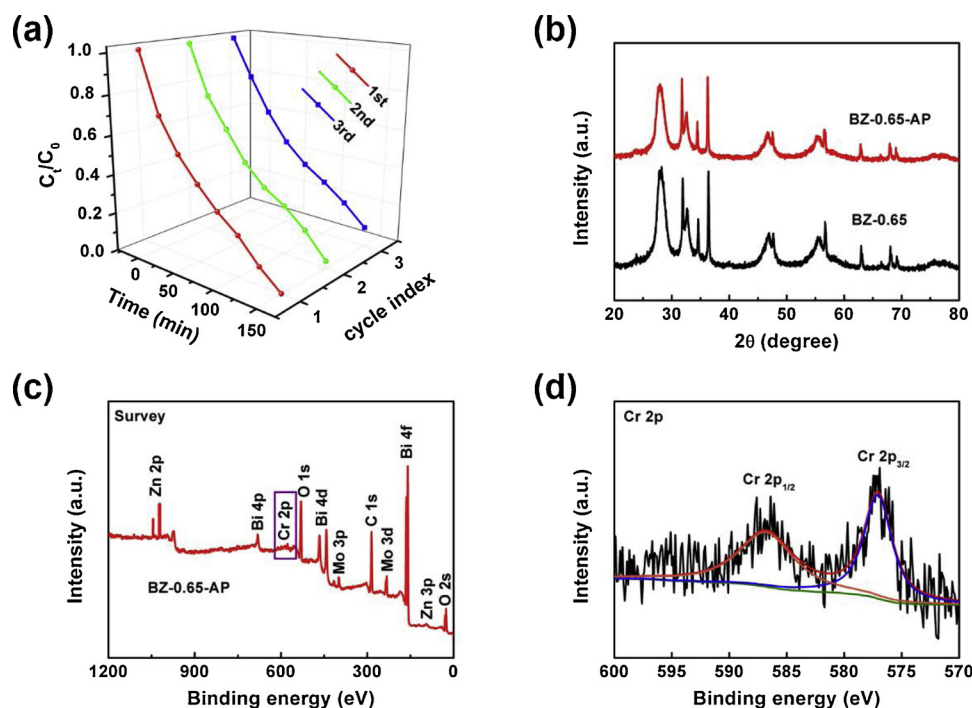

Fig. 11. (a) Cycling experiments of photocatalytic reduction of Cr(VI) over BZ-0.65. (b). XRD patterns of BZ-0.65 and BZ-0.65-AP (BZ-0.65 recovered after three cycles of photocatalysis). XPS analysis of BZ-0.65-AP: (c) survey and (d) Cr 2p spectra.

light irradiation.

3.9. Possible photocatalytic mechanism

Based on the above experimental and characterization data, a possible mechanism of the photocatalytic reduction of Cr(VI) by the Bi_2MoO_6/ZnO composite under visible-light irradiation was proposed, as illustrated in Scheme 2. First, a type-II heterojunction formed when Bi_2MoO_6 was grown on the surface of ZnO because of the suitably matched band structures of Bi_2MoO_6 and ZnO (see Fig. 7). Second, When the Bi_2MoO_6/ZnO composite was excited under visible-light irradiation, the photogenerated electrons were excited from the VB of Bi_2MoO_6 to its CB and the same amount of holes remained in the VB (Equation 8 below). Moreover, because of the formation of a heterojunction between Bi_2MoO_6 and ZnO, and the CB potential of Bi_2MoO_6 is

more active than that of ZnO, the electrons in the CB of Bi_2MoO_6 would transfer rapidly to that of ZnO. As a result, the Bi_2MoO_6/ZnO composite dramatically facilitated the separation of electron–hole pairs compared with the case for the single components, which can lead to more electrons available for photocatalytic reduction of Cr(VI). Third, the Cr(VI)/Cr(III) couple has a reduction potential of + 0.51 eV vs. NHE [42,43]. The CB potentials of Bi_2MoO_6 and ZnO are −0.39 and −0.16 eV (Fig. 5), which are more negative than the reduction potential of the Cr(VI)/Cr(III) couple. From the viewpoint of thermodynamics, it is feasible to photoreduce Cr(VI) to Cr(III) by photogenerated electrons [43]. Finally, $Cr_2O_7^{2-}$ is reduced to Cr(III) by electrons and O_2 is produced by oxidation of H_2O, as summarized in Equation 9 and 10.

$$Bi2MoO6/ZnO + h\nu \rightarrow e^- + h^+ \tag{8}$$

$$Cr_2O_7^{2-} + 14H^+ + 6e^- \rightarrow 2Cr^{3+} + 7H_2O \tag{9}$$
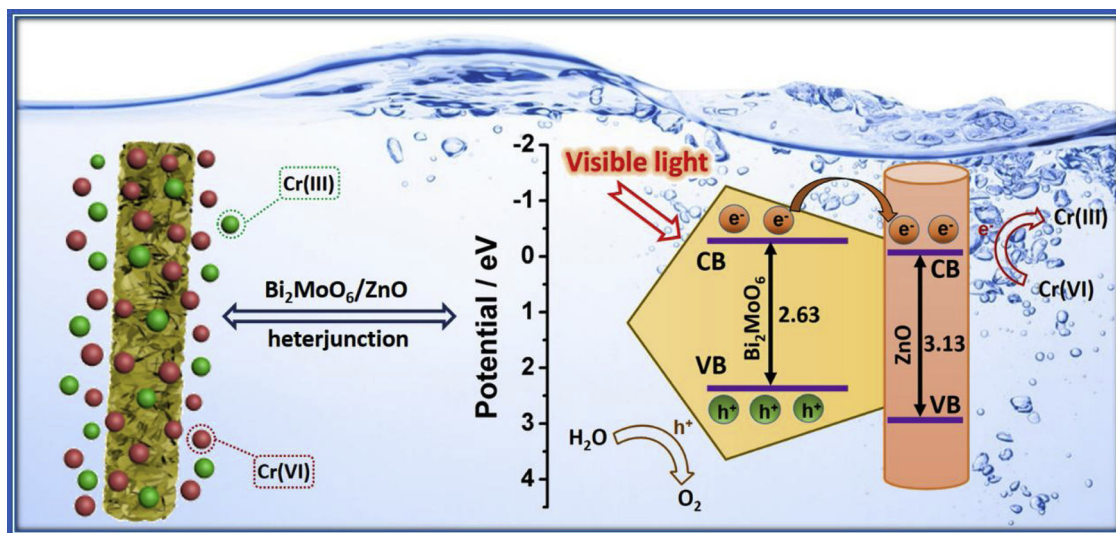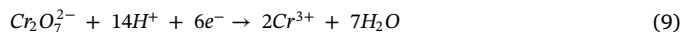
Scheme 2. Schematic illustration of the proposed mechanism of reduction of Cr(VI) over the 3D Bi_2MoO_6/ZnO composite under visible-light irradiation.

322

$$2H_2O + 4h^+ \rightarrow O_2 + 4H^+ \tag{10}$$

4. Conclusion

Visible light-responsive Bi_2MoO_6/ZnO photocatalysts with interfacial contact were synthesized by a solvothermal method. Bi_2MoO_6/ZnO composites with two different morphologies of Bi_2MoO_6 (nanoparticles and nanosheets) were obtained by controlling the precursor concentration. The Bi_2MoO_6/ZnO composites displayed obviously enhanced photocatalytic activity in photoreduction of Cr(VI) compared with those of pure Bi_2MoO_6 and ZnO under visible-light illumination. Photoelectrochemical measurements revealed that the Bi_2MoO_6/ZnO composites displayed a higher photocurrent response and lower electrochemical impedance than those of their individual components, indicating the photogenerated electrons and holes were effectively separated and transferred in the composites. The improved photocatalytic activity and charge separation efficiency of the composites was attributed to the construction of a hierarchical heterojunction between Bi_2MoO_6 and ZnO. The Bi_2MoO_6/ZnO photocatalysts retained good stability after three photocatalytic cycles. This work demonstrated that Bi_2MoO_6/ZnO hierarchical heterostructures are promising photocatalysts for wastewater treatment under solar light.

Acknowledgements

Appendix A. Supplementary data

Supplementary material related to this article can be found, in the online version, at doi:https://doi.org/10.1016/j.apcatb.2019.03.055.

References

[1] X. An, J.C. Yu, F. Wang, C. Li, Y. Li, One-pot synthesis of In_2S_3 nanosheets/graphene composites with enhanced visible-light photocatalytic activity, Appl. Catal. B: Environ. 129 (2013) 80–88.

[2] C.N. Ri, S.G. Kim, K.S. Ju, H.S. Ryo, C.H. Mun, U.H. Kim, The synthesis of a Bi_2MoO_6/$Bi_4V_2O_{11}$ heterojunction photocatalyst with enhanced visible-light-driven photocatalytic activity, RSC Adv. 8 (2018) 5433–5440.

[3] F. Guo, W. Shi, W. Guan, H. Huang, Y. Liu, Carbon dots/g-C_3N_4/ZnO nanocomposite as efficient visible-light driven photocatalyst for tetracycline total degradation, Sep. Purif. Technol. 173 (2017) 295–303.

[4] J. Yu, S. Zhuang, X. Xu, W. Zhu, B. Feng, J. Hu, Photogenerated electron reservoir in hetero-p-n CuO-ZnO nanocomposite device for visible-light-driven photocatalytic reduction of aqueous Cr(VI), J. Mater. Chem. A 3 (2015) 1199–1207.

[5] P.Y. Kuang, J.R. Ran, Z.Q. Liu, H.J. Wang, N. Li, Y.Z. Su, Y.G. Jin, S.Z. Qiao, Enhanced photoelectrocatalytic activity of BiOI nanoplate-zinc oxide nanorod p-n heterojunction, Chem. Eur. J. 21 (2015) 15360–15368.

[6] Y. Wang, R. Shi, J. Lin, Y. Zhu, Enhancement of photocurrent and photocatalytic activity of ZnO hybridized with graphite-like C_3N_4, Energy Environ. Sci. 4 (2011) 2922–2929.

[7] N. Li, Y. Tian, J. Zhao, J. Zhang, W. Zuo, L. Kong, H. Cui, Z-scheme 2D/3D g-C_3N_4@ ZnO with enhanced photocatalytic activity for cephalexin oxidation under solar light, Chem. Eng. J. 352 (2018) 412–422.

[8] N. Li, J. Zhang, Y. Tian, J. Zhao, J. Zhang, W. Zuo, Precisely controlled fabrication of magnetic 3D γ-Fe_2O_3@ZnO core-shell photocatalyst with enhanced activity: ciprofloxacin degradation and mechanism insight, Chem. Eng. J. 308 (2017) 377–385.

[9] C. Wang, H. Lin, Z. Liu, J. Wu, Z. Xu, C. Zhang, Controlled formation of TiO_2/MoS_2 core-shell heterostructures with enhanced visible-light photocatalytic activities, Part. Part. Syst. Charact. 33 (2016) 221–227.

[10] J. Jiang, X. Zhang, P. Sun, L. Zhang, ZnO/BiOI heterostructures: photoinduced charge-transfer property and enhanced visible-light photocatalytic activity, J. Phys. Chem. C 115 (2011) 20555–20564.

[11] S. Adhikari, S. Selvaraj, D.H. Kim, Construction of heterojunction photoelectrode via atomic layer deposition of Fe_2O_3 on Bi_2WO_6 for highly efficient photoelectrochemical sensing and degradation of tetracycline, Appl. Catal. B: Environ. 244 (2019) 11–24.

[12] F. Xu, H. Chen, C. Xu, D. Wu, Z. Gao, Q. Zhang, K. Jiang, Ultra-thin Bi_2WO_6 porous nanosheets with high lattice coherence for enhanced performance for photocatalytic reduction of Cr(VI), J. Colloid. Interface Sci. 525 (2018) 97–106.

[13] J. Ding, Z. Yang, C. He, X. Tong, Y. Li, X. Niu, H. Zhang, UiO-66(Zr) coupled with Bi_2MoO_6 as photocatalyst for visible-light promoted dye degradation, J. Colloid. Interf. Sci. 497 (2017) 126–133.

[14] Y. Tian, F. Zhou, S. Zhan, Z. Zhu, Q. He, Mechanisms on the enhanced sterilization performance of fluorocarbon resin composite coatings modified by g-C_3N_4/Bi_2MoO_6 under the visible-light, J. Photochem. Photobiol. A 350 (2018) 10–16.

[15] J. Zhang, C. Shao, X. Li, J. Xin, R. Tao, Y. Liu, Assembling n-Bi_2MoO_6 nanosheets on electrospun p-$CuAl_2O_4$ hollow nanofibers: enhanced photocatalytic activity based on highly efficient charge separation and transfer, ACS Sustain. Chem. Eng. 6 (2018) 10714–10723.

[16] X.Q. Qiao, Z.W. Zhang, Q.H. Li, D. Hou, Q. Zhang, J. Zhang, D. Li, P. Feng, X. Bu, *In situ* synthesis of n–n Bi_2MoO_6 & Bi_2S_3 heterojunctions for highly efficient photocatalytic removal of Cr(VI), J. Mater. Chem. A 6 (2018) 22580–22589.

[17] X. Tian, S. Qu, B. Wang, Z. Xu, Hydrothermal synthesis and photocatalytic property of Bi_2MoO_6/ZnO composite material, Res. Chem. Intermed. 41 (2015) 7273–7283.

[18] Y. Chen, G. Tian, Z. Ren, K. Pan, Y. Shi, J. Wang, H. Fu, Hierarchical core-shell carbon nanofiber@$ZnIn_2S_4$ composites for enhanced hydrogen evolution performance, ACS Appl. Mater. Interfaces 6 (2014) 13841–13849.

[19] M. Zhang, C. Shao, J. Mu, Z. Zhang, Z. Guo, P. Zhang, Y. Liu, One-dimensional Bi_2MoO_6/TiO_2 hierarchical heterostructures with enhanced photocatalytic activity, Crystengcomm 14 (2012) 605–612.

[20] W. Zhou, Z. Yin, Y. Du, X. Huang, Z. Zeng, Z. Fan, H. Liu, J. Wang, H. Zhang, Synthesis of few-layer MoS_2 nanosheet-coated TiO_2 nanobelt heterostructures for enhanced photocatalytic activities, Small 9 (2013) 140–147.

[21] M. Lu, C. Shao, K. Wang, N. Lu, X. Zhang, P. Zhang, M. Zhang, X. Li, Y. Liu, p-MoO_3 nanostructures/n-TiO_2 nanofiber heterojunctions: controlled fabrication and enhanced photocatalytic properties, ACS Appl. Mater. Interfaces 6 (2014) 9004–9012.

[22] P. Zhang, C. Shao, M. Zhang, Z. Guo, J. Mu, Z. Zhang, X. Zhang, Y. Liu, Bi_2MoO_6 ultrathin nanosheets on $ZnTiO_3$ nanofibers: A 3D open hierarchical heterostructures synergistic system with enhanced visible-light-driven photocatalytic activity, J. Hazard. Mater. 217–218 (2012) 422–428.

[23] S. Li, X. Shen, J. Liu, L. Zhang, Synthesis of Ta_3N_5/Bi_2MoO_6 core-shell fiber-shaped heterojunctions as efficient and easily recyclable photocatalysts, Environ. Sci. Nano 4 (2017) 1155–1167.

[24] L. Zhu, H. Li, P. Xia, Z. Liu, D. Xiong, Hierarchical ZnO decorated with CeO_2 nanoparticles as the direct Z-Scheme heterojunction for enhanced photocatalytic activity, ACS Appl. Mater. Interfaces 10 (2018) 39679–39687.

[25] K. Lai, W. Wei, Y. Dai, R. Zhang, B. Huang, DFT calculations on structural and electronic properties of Bi_2MO_6 (M = Cr, Mo, W), Rare Metals 30 (2011) 166–172.

[26] H. Li, W. Li, S. Gu, F. Wang, X. Liu, C. Ren, Forming oxygen vacancies inside in lutetium-doped Bi_2MoO_6 nanosheets for enhanced visible-light photocatalytic activity, Mol. Catal. 433 (2017) 301–312.

[27] Y. Wang, X. Li, N. Wang, X. Quan, Y. Chen, Controllable synthesis of ZnO nanoflowers and their morphology-dependent photocatalytic activities, Sep. Purif. Technol. 62 (2008) 727–732.

[28] M. Zhang, C. Shao, J. Mu, X. Huang, Z. Zhang, Z. Guo, P. Zhang, Y. Liu, Hierarchical heterostructures of Bi_2MoO_6 on carbon nanofibers: controllable solvothermal fabrication and enhanced visible photocatalytic properties, J. Mater. Chem. 22 (2012) 577–584.

[29] B. Jin, Z. Jiao, Y. Bi, Efficient charge separation between Bi_2MoO_6 nanosheets and ZnO nanowires for enhanced photoelectrochemical properties, J. Mater. Chem. A 3 (2015) 19702–19705.

[30] J. Lv, J. Zhang, J. Liu, Z. Li, K. Dai, C. Liang, Bi SPR-Promoted Z-Scheme Bi_2MoO_6/CdS-Diethylenetriamine composite with effectively enhanced visible light photocatalytic hydrogen evolution activity and stability, ACS Sustain. Chem. Eng. 6 (2018) 696–706.

[31] J.X. Sun, Y.P. Yuan, L.G. Qiu, X. Jiang, A.J. Xie, Y.H. Shen, J.F. Zhu, Fabrication of composite photocatalyst g-C_3N_4-ZnO and enhancement of photocatalytic activity under visible light, Dalton Trans. 41 (2012) 6756–6763.

[32] F. Zhang, Y. Zhang, C. Zhou, Z. Yang, H. Xue, D.D. Dionysiou, A new high efficiency visible-light photocatalyst made of SnS_2 and conjugated derivative of polyvinyl alcohol and its application to Cr(VI) reduction, Chem. Eng. J. 324 (2017) 140–153.

[33] S. Patnaik, G. Swain, K.M. Parida, Highly efficient charge transfer through a double Z-scheme mechanism by a Cu-promoted MoO_3/g-C_3N_4 hybrid nanocomposite with superior electrochemical and photo catalytic performance, Nanoscale 10 (2018) 5950–5964.

[34] L. Xu, X. Bai, L. Guo, S. Yang, P. Jin, L. Yang, Facial fabrication of carbon quantum dots (CDs)-modified N-TiO_2-x nanocomposite for the efficient photoreduction of Cr (VI) under visible light, Chem. Eng. J. 357 (2019) 473–486.

[35] J. Liu, Y. Zhao, J. Ma, Y. Dai, J. Li, J. Zhang, Flower-like ZnO hollow microspheres on ceramic mesh substrate for photocatalytic reduction of Cr(VI) in tannery wastewater, Ceram. Int. 42 (2016) 15968–15974.

[36] F. Zhang, Y. Zhang, G. Zhang, Z. Yang, D.D. Dionysiou, A. Zhu, Exceptional synergistic enhancement of the photocatalytic activity of SnS_2 by coupling with polyaniline and N-doped reduced graphene oxide, Appl. Catal. B: Environ. 236 (2018) 53–63.

[37] X. Hu, X. Wang, G. Xie, H. Wang, X. Tan, Q. Jin, D. Zhou, Y. Zhao, Ternary assembly of g-C_3N_4/graphene oxide sheets /$BiFeO_3$ heterojunction with enhanced

photoreduction of Cr(VI) under visible-light irradiation, Chemosphere 216 (2019) 733–741.

[38] D. Xiao, K. Dai, Y. Qu, Y. Yin, H. Chen, Hydrothermal synthesis of α-Fe₂O₃/g-C₃N₄ composite and its efficient photocatalytic reduction of Cr(VI) under visible light, Appl. Surf. Sci. 358 (2015) 181–187.

[39] N. Wang, L. Zhu, Y. Huang, Y. She, Y.U. Yanmin, H. Tang, Drastically enhanced visible-light photocatalytic degradation of colorless aromatic pollutants over TiO₂ via a charge-transfer-complex path: a correlation between chemical structure and degradation rate of the pollutants, J. Catal. 266 (2009) 199–206.

[40] Y.C. Zhang, J. Li, H.Y. Xu, One-step in situ solvothermal synthesis of SnS₂/TiO₂ nanocomposites with high performance in visible light-driven photocatalytic

[41] Y.C. Zhang, L. Yao, G. Zhang, D.D. Dionysios, J. Li, X.H. Du, One-step hydrothermal synthesis of high-performance visible-light-driven SnS₂/SnO₂ nanoheterojunction photocatalyst for the reduction of aqueous Cr(VI), Appl. Catal. B: Environ. 144 (2014) 730–738.

[42] R. Liang, L. Shen, F. Jing, W. Wu, N. Qin, R. Lin, L. Wu, NH₂-mediated indium metal–organic framework as a novel visible-light-driven photocatalyst for reduction of the aqueous Cr(VI), Appl. Catal. B: Environ. 162 (2015) 245–251.

[43] W. Huang, N. Liu, X. Zhang, M. Wu, L. Tang, Metal organic framework g-C₃N₄/MIL-53(Fe) heterojunctions with enhanced photocatalytic activity for Cr(VI) reduction under visible light, Appl. Surf. Sci. 425 (2017) 107–116.

reduction of aqueous Cr(VI), Appl. Catal. B: Environ. 123–124 (2012) 18–26.